

Urbanization Enhanced Summertime Extreme Hourly Precipitation over the Yangtze River Delta

XIAOLING JIANG

State Key Laboratory of Severe Weather, Chinese Academy of Meteorological Sciences, and University of Chinese Academy of Sciences, Beijing, China

YALI LUO

State Key Laboratory of Severe Weather, Chinese Academy of Meteorological Sciences, Beijing, and Collaborative Innovation Center on Forecast and Evaluation of Meteorological Disasters, Nanjing University of Information Science and Technology, Nanjing, China

DA-LIN ZHANG

State Key Laboratory of Severe Weather, Chinese Academy of Meteorological Sciences, Beijing, China, and Department of Atmospheric and Oceanic Science, University of Maryland, College Park, College Park, Maryland

MENGWEN WU

Zhejiang Institute of Meteorological Sciences, Zhejiang Meteorological Bureau, Hangzhou, China

(Manuscript received 26 November 2019, in final form 2 April 2020)


ABSTRACT

An extensive urban agglomeration has occurred over the Yangtze River delta (YRD) region of East China as a result of rapid urbanization since the middle 1990s. In this study, a 44-yr (i.e., 1975–2018) climatology of the summertime extreme hourly precipitation (EXHP; greater than the 90th percentile) over the YRD is analyzed, using historical land-use data, surface temperature, and hourly rain gauge observations, and then the relationship between rapid urbanization and EXHP changes is examined. Results show significant EXHP contrasts in diurnal variation and storm type roughly before and after middle July. That is, tropical cyclones (TCs) account for 16.4% of the total EXHP hours, 80.5% of which occur during the late summer, whereas non-TC EXHP accounts for 94.7% and 66.2% during the early and late summer, respectively. Increasing trends in occurrence frequency and amount of the non-TC and TC-induced EXHP are detected over the urban agglomeration. Statistically significant larger increasing trends in both the EXHP and surface temperature are observed at urban stations than those at the nearby rural stations. An analysis of 113 locally developed non-TC extreme rainfall events during 2011–18 summers also suggests the contribution of the urban heat island effects to the more occurrences of EXHP, especially over a band-shaped urban region where several major cities are distributed. This study reveals a significant correlation between rapid urbanization and increased EXHP during the past two decades over the YRD region. The results have important implications for understanding the impact of urbanization on EXHP changes in a warming climate.

1. Introduction

Rapid urbanization since the early-to-middle 1990s has led to the formation of three major urban agglomerations in China, namely the Beijing–Tianjin–Hebei

(BTH) area in North China, the Pearl River delta (PRD) in coastal South China, and the Yangtze River delta (YRD) in coastal East China. The YRD urban agglomeration consists of a band-shaped city region extending from the Shanghai (SH) municipality northwestward along the Yangtze River sequentially to Suzhou (SZ), Wuxi (WX), Changzhou (CZ), and Nanjing (NJ), and two relatively smaller city areas to its south centered around Hangzhou (HZ) and Ningbo (NB), respectively (see Fig. 1a for their locations). Substantial modifications have been made to the surface properties during

 Denotes content that is immediately available upon publication as open access.

Corresponding author: Dr. Yali Luo, ylluo@cma.gov.cn, yali.luo@qq.com

DOI: 10.1175/JCLI-D-19-0884.1

© 2020 American Meteorological Society. For information regarding reuse of this content and general copyright information, consult the [AMS Copyright Policy](https://www.ametsoc.org/PUBSReuseLicenses) (www.ametsoc.org/PUBSReuseLicenses).

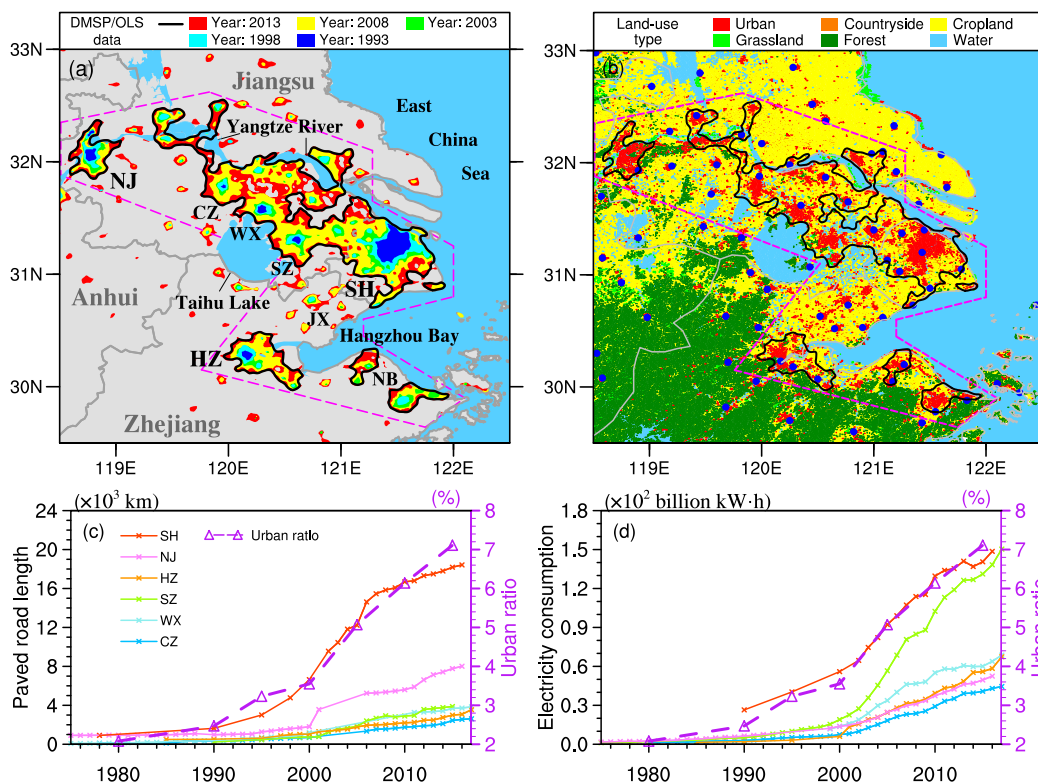


FIG. 1. (a) Urban areas (color shadings) in the Yangtze River delta region identified with the DMSP/OLS nighttime light data in the five years of 1993 (blue), 1998 (cyan), 2003 (green), 2008 (yellow), and 2013 (red). (b) Land-use types over the YRD in 2015 and the locations of 70 national surface stations (large blue dots). The solid black line represents the boundaries of contiguous urban areas in 2013–15. Dashed pink lines, used in many figures that follow (i.e., Figs. 2, 3, 7, 8, 10, 12, and 13), denote the key analysis area covering most urban areas that are contiguous or scattered nearby. (c) Evolution of urbanization reflected by paved road length (10^3 km) in the six major cities over the YRD region, namely, Nanjing (NJ), Changzhou (CZ), Wuxi (WX), and Suzhou (SZ) in the Jiangsu Province, Hangzhou (HZ) in the Zhejiang Province, and the Shanghai (SH) metropolitan, and the urban ratio (%) within the YRD region based on the land-use data. (d) As in (c), but for electricity consumption (10^2 billion kWh) and urban ratio (%).

the past several decades; for example, grass and croplands were replaced by artificial surfaces like concrete and tall buildings over the YRD (Fig. 1b). The resultant urban heat island (UHI) and urban canopy effects could contribute to changes in local and regional atmospheric circulations and precipitation (Shepherd and Burian 2003; Shepherd 2005; Kaufmann et al. 2007; Kishtawal et al. 2010; Yu et al. 2016; Zhang et al. 2019; Zhang 2020). In recent years, precipitation has remarkably increased over the midlower reaches of the Yangtze River valley (Yu et al. 2010). Seven out of the top 10 hourly precipitation extremes over the YRD during 1975–2018 summers occurred in and after 1995 (Table 1). Heavy precipitation, especially associated with extreme events, tends to induce floods and waterlogging, causing severe economic losses and casualties over the Yangtze River valley (NCC 1998; Zhang et al. 2005).

Numerous studies have investigated changes in intensity and distribution of precipitation over densely populated vulnerable city areas and their relationship to urbanization over the world. Changnon (1968, 1969) was among the first to find an increase in total precipitation over La Porte, a city to the east of Chicago, which was indicated as a result of urbanization. Subsequent studies observed increasing trends in heavy rainfall events associated with urbanization (e.g., Shepherd and Burian 2003; Kishtawal et al. 2010; Niyogi et al. 2011; Mishra et al. 2012; Shastri et al. 2015). Urbanization could also cause spatial variability of regional rainfall, which in turn primes atmospheric setting for intensification of urban rainfall (Paul et al. 2018). Upstream urbanization could exacerbate UHI effects and cascade downwind (D.-L. Zhang et al. 2009; Wan et al. 2013; Zhang and Chen 2014) that are favorable for convective initiation (Li et al. 2017b), leading to more precipitation occurring

TABLE 1. The top 10 hourly precipitation rates (mm h^{-1}) at the national stations over the YRD region (see Fig. 1b for their distributions) during 1975–2018 summers.

No.	Year	Month	Day	Hour	City	Precipitation
1	1991	8	7	23	Shanghai	119.6
2	2008	8	25	7	Shanghai	117.5
3	2011	8	25	13	Jiaxing	111.9
4	1995	8	28	17	Zhenjiang	109.9
5	1997	8	13	19	Jiaxing	108.8
6	1985	7	26	10	Chuzhou	108.7
7	1995	6	21	4	Nantong	105.2
8	2011	6	24	15	Wuxi	101.3
9	1977	8	10	18	Nantong	100.3
10	1997	8	13	18	Jiaxing	96.9

over downtown and downwind of large cities (Shepherd and Burian 2003; Zhang et al. 2018; Zhang 2020). Recent studies suggest that precipitation intensity and pattern changes over urban agglomerations in China depend on geographical locations and regional climate regimes (Fu et al. 2019). Specifically, significant positive trends are detected in the amounts and occurrence frequencies of extreme precipitation events in the Pearl River basin over South China (Q. Zhang et al. 2009; Li et al. 2011), with larger increasing frequency of extreme hourly precipitation (EXHP) over the PRD urban agglomeration during the rapid urbanization period (about 1994–2016) than during the preurbanization era (from 1971 to about 1993) (Wu et al. 2019). A distinct “rain island” feature is observed in the megacity of Shanghai during the rapid urbanization period, with extreme hourly precipitation being enhanced significantly and concentrated over the urban and suburban areas (Liang and Ding 2017). However, statistically insignificant positive or negative trends are noticed in the extreme (greater than the 95th percentile) and annual maximal hourly precipitation over the BTH during 1971–2013 (Xiao et al. 2016), where urban expansion could even contribute to summer rainfall reduction because of less surface evaporation, higher surface temperature, and less water vapor (C. Zhang et al. 2009; Zhang et al. 2014).

The previous studies mainly used daily or monthly rainfall datasets (e.g., Shepherd and Burian 2003; Zhai et al. 2005; C. Zhang et al. 2009; Q. Zhang et al. 2009; Zhang et al. 2014). However, extreme precipitation is often confined to a few hours and even periods shorter than one hour (Yu et al. 2010). Current understanding of the characteristics and changes of subdaily precipitation extremes is very limited in general (Zhang et al. 2017), and even less over urban environments because of the complicated interactions and sometimes compensating effects of nearby cities, namely, the UHI-induced destabilization (Lei et al. 2008; Lin et al. 2011; Li et al.

2017b; Yang et al. 2017), building barrier of urban canyons (C. Zhang et al. 2009; Miao et al. 2011; Zhong and Yang 2015; Zhang et al. 2018, 2019), and anthropogenic aerosol emissions for cloud condensation nuclei sources (Rosenfeld 2000; Jin and Shepherd 2008; Ntelekos et al. 2009; Zhong et al. 2015). Moreover, the extensive urban agglomeration over the YRD consists of numerous larger and smaller urban areas (Figs. 1a,b) with a “chain flow” by downstream propagation of the UHI signal (D.-L. Zhang et al. 2009; Wan et al. 2013). Therefore, it is more meaningful to consider the urban agglomeration as a whole, instead of individual cities, in studying the characteristics and changes of EXHP, and their possible link to urbanization over the YRD.

In this study, hourly precipitation observations from surface stations during 1975–2018 are used to study the climatology and trends of EXHP in summer [June–August (JJA)] over the YRD region (118.5° – 122.5° E, 29.5° – 33.0° N). The objectives of this paper are 1) to reveal a climatology of the spatiotemporal distribution of EXHP over the YRD region, 2) to explore changes in EXHP during the past 44 years (i.e., nearly half a century), and 3) to examine the possible association between the observed EXHP changes and urbanization.

The next section describes datasets and analysis methods used in this study. Section 3 presents a 44-yr climatology of the characteristics of EXHP during the JJA of 1975–2018. Section 4 examines whether or not rapid urbanization since the middle 1990s has influenced the summertime EXHP characteristics over the YRD region. Section 5 compares two ensembles of extreme rainfall events occurred with a strong and weak UHI, respectively, during the 2011–18 summers. A summary and concluding remarks are presented in the final section.

2. Data and methodology

a. Analysis region and urbanization background

Located in the coastal region of East China, the YRD urban agglomeration borders the Shanghai metropolitan with the provinces of Jiangsu and Zhejiang to the north and south, respectively (Figs. 1a,b). The urban growth over the YRD region is identified herein by using the satellite nighttime light dataset, historical land-use data, and statistical data of paved road length and electricity consumption. To analyze the version-4 satellite-based nighttime light data from the Defense Meteorological Satellite Program’s Operational Linescan System (DMSP/OLS) during 1993–2013 (from the National Geophysical Data Center at National Oceanic and Atmospheric Administration; <https://ngdc.noaa.gov/eog/dmsp/downloadV4composites.html>), the digital number

(DN) values of 53, 50, 54, 53, and 53 are used as the urban thresholds for the years of 1993, 1998, 2003, 2008, and 2013, respectively (Fig. 1a), following Wang et al. (2013). Note that different thresholds for the five years are used because the satellites used for the product vary among the years. The boundaries of the continuous urban areas are presented by the contours derived from the DMSP/OLS data in 2013 and used hereafter.

This study also uses the historical land-use data with horizontal resolution of 1 km including seven land-use types: croplands, forest, grasslands, water bodies, countryside, built-up lands, and others (from the Resources and Environment Scientific Data Center, Chinese Academy of Sciences; <http://www.resdc.cn/data.aspx?DATAID=98>). These data have been widely used in studies focusing on, for example, land resource surveys (e.g., Liu et al. 2014; Li et al. 2015) and the rainfall–urbanization relationship (Wu et al. 2019). The land-use data of 2015 agree well with the DMSP/OLS data of 2013 in representing the major urban areas (Fig. 1b). Note that the land-use data show the presence of many smaller urban areas, such as those lying along the Hangzhou Bay between Shanghai and Hangzhou, and those scattered around the Nanjing–Shanghai corridor, which have all contributed to the YRD’s urbanization growth. Therefore, a polygon (bounded by dashed pink lines in Figs. 1a and 1b) covering the contiguous and most scattered urban areas is defined as the key analysis area.

The temporal variations of paved road length and electricity consumption (data from Jiangsu, Zhejiang, and Shanghai Bureau of Statistics; <http://tj.jiangsu.gov.cn/index.html>; <http://tjj.zj.gov.cn/>; <http://tjj.sh.gov.cn/>) clearly show rapid increases in both variables since roughly the mid-1990s at the six major cities, especially Shanghai, Nanjing, and Suzhou, which is consistent with the rapid increase of urban land use. The urban land use is illustrated using the urban ratio calculated as the number of urban grids divided by the number of all grids over the YRD region (Figs. 1c,d). This indicates that the YRD region has undergone rapid urbanization since the mid-1990s. To facilitate understanding the impact of urbanization on the summertime EXHP production, the periods of 1975–96 and 1997–2018 are defined herein as the eras of preurbanization and rapid urbanization, respectively.

b. Data and methodologies for EXHP analysis

A rain gauge–based hourly precipitation dataset from 70 national surface stations (see blue dots in Fig. 1b) during JJA in 1975–2018 is used to analyze the characteristics and changes of EXHP in relation to urbanization over the YRD region. In addition, a homogenized daily surface air temperature (T_{sair}) dataset (Cao et al. 2016) is utilized to analyze how the UHI effects change

during this study period. Both datasets are quality-controlled by the National Meteorological Information Center (NMIC) of the China Meteorological Administration (CMA; <http://data.cma.cn/data/online.html?t=1>), and have been widely used in previous climatological studies (e.g., Yu et al. 2010; Yuan et al. 2010; Zhang and Zhai 2011; Luo et al. 2016; Chen et al. 2018). The national surface stations used in this study have over 90% of reliable hourly data during each JJA of 1975–2018. The Cressman (1959) interpolation method is used to obtain grid point values from station observations.

For each of the 70 stations, a “wet hour” is defined as an hour of measurable precipitation ($\geq 0.1 \text{ mm h}^{-1}$). With this definition, the 90th percentile of hourly precipitation at each station is used as the threshold of EXHP for the station. Higher thresholds such as the 95th and 97.5th percentiles are also tested, and qualitatively similar results are derived. The 90th percentile thresholds increase from about 5 mm h^{-1} at the southeast to about 8 mm h^{-1} at the northwest of the YRD region (Fig. 2b). The amount and occurrence frequency of EXHP are calculated as the accumulated EXHP amount and the number of EXHP hours, respectively. The EXHP intensity is computed as the mean precipitation rate averaged over the EXHP hours. Moreover, an EXHP event at each station in the analysis of 1975–2018 climatology is defined as a time period, when at least one EXHP record occurs, with no intermittence of wet hours or with intermittences lasting less than two continuous hours. The duration of an EXHP event is defined as the number of hours from the beginning to the end of the event. The trends in T_{sair} and precipitation amount, occurrence frequency, and intensity, are estimated using ordinary least squares (OLS) linear regression with an F test. Quantile regression, another linear regression method that could provide a more complete statistical view of the dependent variables in terms of quantiles (Koenker and Bassett 1978) and has been widely used in previous studies (e.g., Friederichs and Hense 2007; Shastri et al. 2015), is performed to further verify the estimated OLS trends in precipitation.

As the daily extreme rainfall induced by tropical cyclones (TCs) exhibits different trends from those of locally induced (Chang et al. 2012), this study identifies the hourly precipitation generated by TCs with the objective synoptic analysis technique (OSAT) developed by Ren et al. (2006, 2007). The OSAT method traces daily rain belts produced by TCs using the distances from their centers and the closeness and continuity between neighboring raining stations. All of the hourly precipitation records in the identified TC rainbelts are termed as TC-induced, whereas all of the other records are termed as non-TC precipitation. The latter is produced

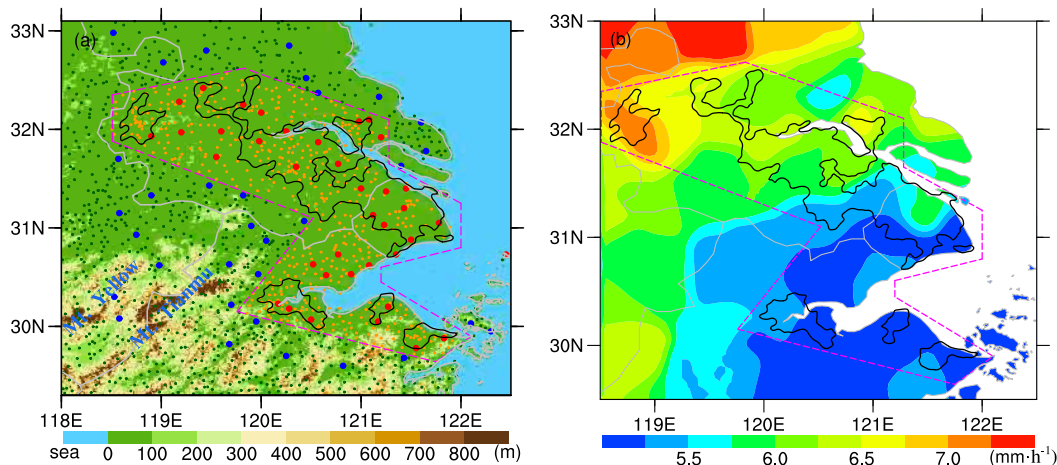


FIG. 2. (a) Spatial distributions of surface stations over the YRD region: the 70 national surface stations (large red and blue dots for stations inside and outside the key analysis area, respectively), the AWSs (small orange and green dots for stations inside and outside the key analysis area, respectively), with shadings denoting topography (m). Mt. Yellow and Mt. Tianmu are labeled. (b) Spatial distribution of the threshold of the EXHP (mm h^{-1}) defined using the 90th percentile.

in close proximity of low-level shear lines and vortices along mei-yu fronts, or far away from such systems mainly in association with near-surface instability due to surface heating (Luo et al. 2016).

To help understand the possible relationship between EXHP changes and UHI effects, extreme rainfall events (EXREs) that occurred over the key analysis area during JJA of 2011–18 are further examined in section 5. In addition to the observations from the national surface stations described earlier, quality-controlled hourly observations of precipitation and $T_{\text{saïr}}$ at the densely distributed automatic weather stations (AWSs) (Fig. 2a) with more than 90% of reliable hourly data during each JJA from 2011 to 2018, provided by the NMIC, are also used to better identify the finescale features in the distributions of UHI and rainfall. Over the regions inside and outside of the key analysis area, there are 632 and 873 stations with precipitation observations (Fig. 2a), among which 558 and 493 stations have temperature observations, respectively. Unlike the definition of EXHP, an EXRE is defined herein as a rainy event with at least one record of hourly precipitation ≥ 23.7 mm at any of the stations over the key analysis area. The EXRE starts from the hour when the key-area-averaged rain accumulation becomes ≥ 0.1 mm and ends at the hour after which the key-area-averaged rainfall remains < 0.1 mm for at least two continuous hours. The 10-min mosaic radar images over the YRD are adopted to further verify the reliability of the extreme rainfall records and to characterize the life cycle of each EXRE based on radar reflectivity. The threshold of 23.7 mm h^{-1} is the

99th percentile of measurable hourly precipitation (≥ 0.1 mm) during the 2011–18 summers at all stations, including both the national-level stations and dense AWSs, over the key analysis area. Using this much higher threshold than that used in the 1975–2018 EXHP analysis, 113 locally developed, non-TC EXREs are identified, with little rainfall during at least 6 h prior to their onsets, so the pre-event UHI intensity (UHII) can be much more clearly estimated. An EXRE may include several extreme hourly records at different stations at one time or another.

The UHII is estimated as the surface temperature difference between urban and rural areas, as in previous studies such as Yang et al. (2017) and Wu et al. (2019), using the following formula:

$$\text{UHII} = T_u - T_r. \quad (1)$$

Here the urban temperature T_u is the hourly $T_{\text{saïr}}$ averaged inside the key analysis area (red and orange dots in Fig. 2a), while the rural temperature T_r is the $T_{\text{saïr}}$ averaged outside the key analysis area (blue and green dots in Fig. 2a). Stations with altitudes higher than 100 m above the mean sea level are excluded in the calculation to avoid the differences in surface temperature caused by different elevations. We calculated the historical mean UHII ($\text{UHII}_{\text{mean}}$) during JJA of 2011–18 as about 0.55°C . During the three hours prior to an EXRE onset, if the UHII of at least two hours exceeds $\text{UHII}_{\text{mean}}$, the EXRE is considered as a strong-UHI event. Otherwise, it is a weak-UHI event.

To examine the spatial distribution of the pre-event UHI for the identified two ensembles of EXREs (i.e., a strong- and a weak-UHI event), the $T_{\text{sa}}^{\text{air}}$ perturbation (ΔT) at each station is calculated as a deviation from the spatial average of $T_{\text{sa}}^{\text{air}}$ over the YRD region for each hour before each EXRE's onset. This method can mostly remove diurnal and seasonal variations of $T_{\text{sa}}^{\text{air}}$, which is required by the composite analysis for each ensemble of the EXREs. Moreover, distributions of the normalized rainfall (NR) are compared between the strong- and weak-UHI EXREs, and NR at each station is calculated by

$$\text{NR} = \frac{R - \bar{R}_{\text{region}}}{\bar{R}_{\text{region}}}, \quad (2)$$

where R is rainfall accumulation of all EXREs (in the strong- or weak-UHI ensembles) at each station; \bar{R}_{region} is the rainfall accumulation averaged over all the stations over the YRD region. This method is useful for describing the local variations of rainfall distributions (Yu 2007; Dou et al. 2015). The 975-hPa horizontal wind field from the ERA-Interim reanalysis data is used to indicate the occurrences of the EXREs with respect to the prevailing airstreams across the urban regions under study.

3. A 44-yr climatology of the total summer precipitation and EXHP

In this section, we present a 44-yr climatology of the total precipitation and EXHP during the summer months over the YRD region. Figure 3 shows spatial distributions of the averaged amount and occurrence frequency of the total summer precipitation and the EXHP over the YRD region during the JJA of 1975–2018. The total precipitation amount peaks (>640 mm) in the southwest of the YRD region, where complex terrain (e.g., Mt. Yellow and Mt. Tianmu) is distributed (cf. Figs. 3a and 2a), and this is consistent with that found by Fu et al. (2019). The upper and lower portions of the key analysis area covering the urban areas have precipitation amounts of about 500 and 540 mm, respectively, with a minimum of about 480 mm in between. The number of wet hours generally decreases with latitude over the YRD region, with high occurrence frequencies in the southwest and southeast, in good agreement with the distribution of total precipitation amount (cf. Figs. 3b and 3a). A comparison of Figs. 3c,d and 3a,b shows that spatial distributions of the amount and occurrence frequency of EXHP present similar patterns to those of the total precipitation, but different in magnitude. A high correlation between

larger amount or higher occurrence frequency of precipitation and urban areas is not observed. This appears to be attributable to the impact of topography on the upstream of prevailing southwesterly monsoonal air at the southwest, namely, removing large moisture content that may be otherwise used for precipitation over the downstream urban regions.

A total of 60 218 (83.6%) and 11 828 (16.4%) non-TC and TC-induced EXHP hours, respectively, are found during the 1975–2018 summers (Table 2). Diurnal and every-10-day variations in the EXHP hours, and durations of the corresponding EXHP events (defined in section 2b), are comparatively examined for the pairs of EXHP-related parameters (Fig. 4). Note that about 69.0% of the non-TC EXHP hours occur during early June to 20 July (approximately the mei-yu season; Ding 1992), and the remaining 31.0% take place during late July to the end of August (i.e., the post-mei-yu period). The non-TC EXHP hours during the periods of mei-yu and post-mei-yu accounts for 94.7% and 66.2% of all the EXHP hours during each period, respectively (Table 2). More than half (57.6%) of the post-mei-yu non-TC EXHP hours take place in the afternoon-to-evening hours [1200–2300 local solar time (LST)] with short durations (i.e., ≤ 12 h) (Figs. 4a,b), resulting likely from surface heating. In contrast, a comparable fraction (30.0%) of the non-TC EXHP hours during the mei-yu season occur in the nocturnal-to-morning hours (0000–1100 LST) with longer durations (>12 h), but they rarely occur in late summer. This appears to reflect the important roles played by the low-level southwesterly monsoonal flow and the boundary layer inertial oscillation of ageostrophic winds, leading to the formation of low-level jets (LLJs), in providing net moisture flux into the YRD region for the nocturnal-to-morning EXHP production (Luo et al. 2018).

By comparison, about 80.5% of the TC-induced EXHP hours occur during the post-mei-yu period, accounting for about one-third (i.e., 33.8%) of all the EXHP hours for the period. About a half (47.6%) of these EXHP events last 1–12 h, while about 24.8% persist longer than one day (Figs. 4e,f). Like the non-TC EXHP during the post-mei-yu period, diurnal variation of the TC-induced EXHP exhibits a prominent late-afternoon (1600–1700 LST) peak occurring with mostly short durations (i.e., ≤ 12 h) (cf. Figs. 4c,f). This result suggests that surface heating could intensify hourly precipitation under the favorable influence of TC circulations (i.e., ample moisture supply and persistent upward motion).

Of interest is the double peaks in the diurnal variations of occurrence frequency of the non-TC EXHP, with a major peak in the afternoon (1400–1800 LST)

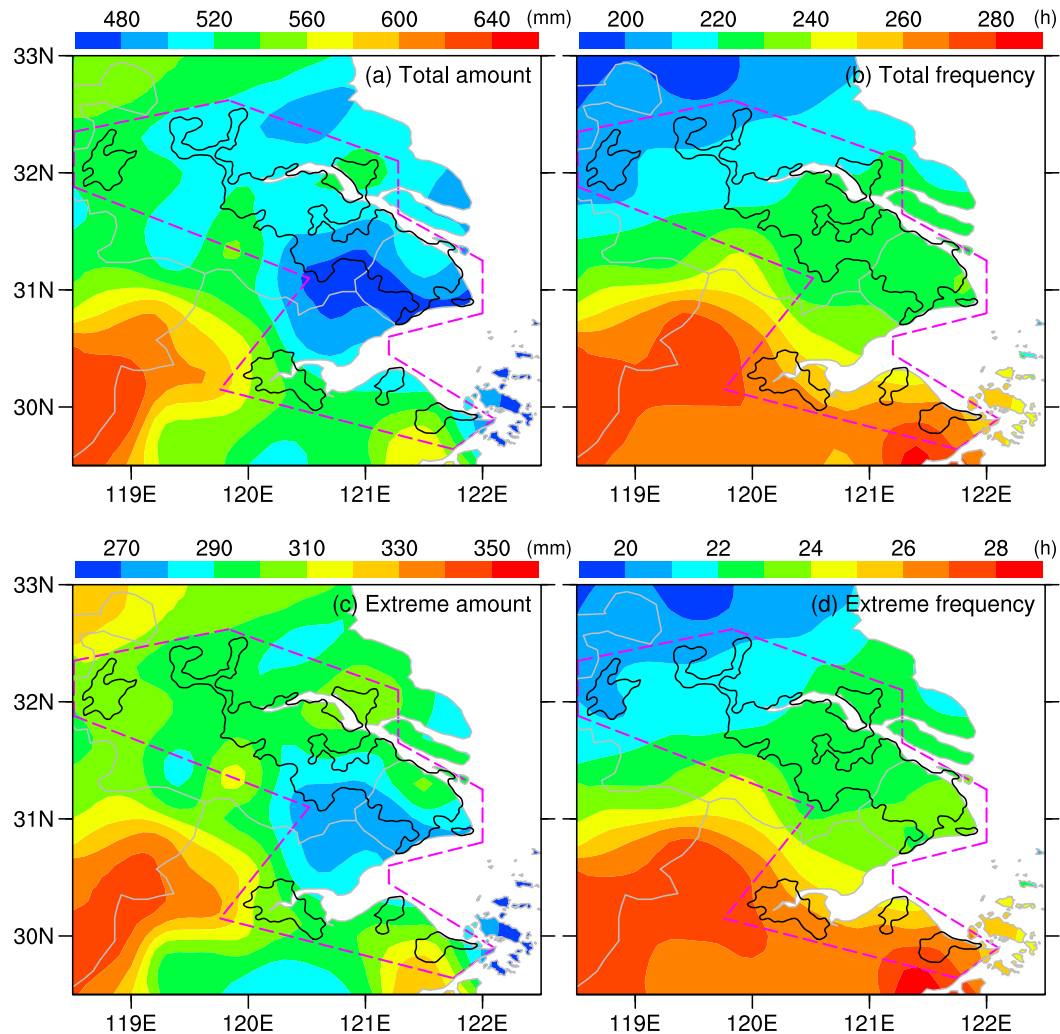


FIG. 3. Spatial distribution of the summer-mean precipitation during 1975–2018: (a) amount (mm) and (b) occurrence frequency (h) of the total precipitation. (c),(d) As in (a) and (b), respectively, but for the EXHP.

and a secondary peak in the morning (0600–0900 LST) (Figs. 5 and 4a). In contrast, the occurrence frequency of the TC-induced EXHP has a single peak in the afternoon period (1500–1700 LST) (Figs. 5 and 4d), which is qualitatively consistent with the previous finding that TC-produced precipitation has a maximum in the afternoon over land, but a maximum in the early morning over ocean (Tuleya 1994; Bowman and Fowler 2015). The prominent late-afternoon peak of both the non-TC and TC-induced EXHP results from the surface heating-induced instability.

Figure 5 also shows the diurnal variations of occurrence frequency of all the EXHP (i.e., including both the non-TC and TC-induced EXHP) during the mei-yu and post-mei-yu periods, respectively. Results reveal that the above-mentioned double peaks occur mostly during

the mei-yu period reflecting likely the collective roles of nocturnal-to-morning LLJs and daytime solar heating, whereas those in the post-mei-yu period features with a single late-afternoon peak. These are consistent with that shown in the previous studies of mean precipitation and convection over the middle and lower reaches of Yangtze River (e.g., Xu and Zipser 2011; Luo et al. 2013).

4. Relationship between EXHP changes and urbanization

In this section, we analyze the EXHP changes during the past four decades and examine whether they could be related to rapid urbanization. While a high correlation between larger amount or higher frequency of

TABLE 2. The occurrence frequency (h) of EXHP during the 1975–2018 summers.

	Summer	1 Jun–20 Jul	21 Jul–31 Aug
All EXHP	72 046	43 867	28 179
Non-TC EXHP	60 218	41 560	18 658
TC-induced EXHP	11 828	2307	9521

precipitation and urban areas is not observed, both the total precipitation and the EXHP amount, as shown in Fig. 6, have increased during 1975–2018 with statistically significant trends of 2.9 and 2.3 mm yr⁻¹ (at 90% and 99% confidence levels), respectively. This appears to coincide with the rapid urbanization over the YRD region (cf. Figs. 6 and 1c,d). Moreover, although the decadal variations could be associated with the “southern flood–northern drought” phenomenon of the East Asian summer monsoon rainfall (e.g., Yu et al. 2010), these positive trends are qualitatively consistent with thermodynamic consequence of global warming and can also be contributed by the local urban agglomeration effects, especially the UHI effects.

To help explore the relationship between urbanization and the EXHP changes, Fig. 7 compares spatial distributions of the amount, occurrence frequency, and intensity of the summer EXHP between the earlier and later 22 years (i.e., the preurbanization and rapid urbanization eras). During the preurbanization era (i.e., 1975–96), the key analysis area features lower EXHP amounts (Fig. 7a), whereas during the rapid urbanization era there are locations of higher EXHP amounts (Fig. 7b) and remarkable increases are observed (Fig. 7c). Note that a localized EXHP center is located in central Shanghai during both eras (Figs. 7a,b), which is consistent with the finding of Liang and Ding (2017), who attributed this feature to the impact of urbanization. Note also that the EXHP occurrence frequency decreases generally with latitude during the preurbanization era (Fig. 7d). However, a different scenario is seen during the rapid urbanization era, with more occurrences of EXHP (Fig. 7e) and notable increases in the EXHP occurrence frequency (Fig. 7f) over the key analysis area. The EXHP intensity increases with latitude during both eras with the strongest EXHP in the north (Figs. 7g,h) where the EXHP occurs the least frequently

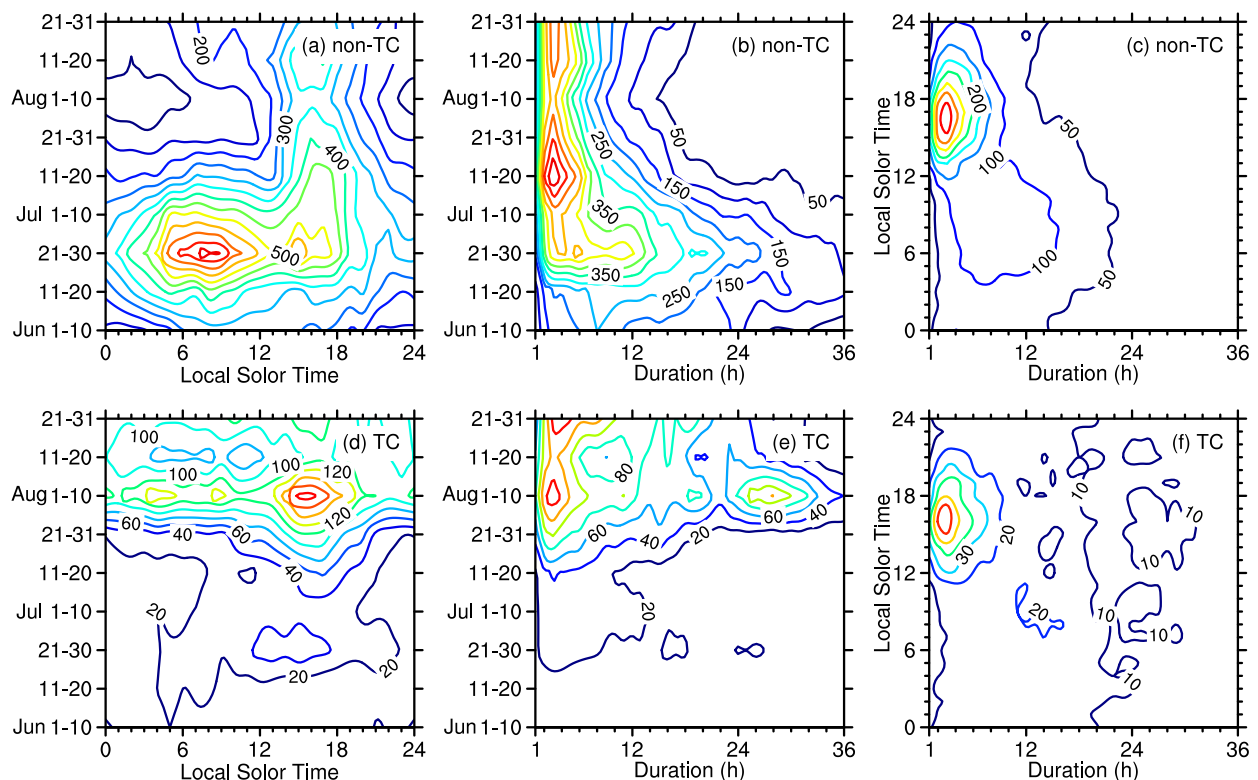


FIG. 4. Two-dimensional distributions of the occurrence frequency (h) of the non-TC EXHP during the 1975–2018 summers: (a) local solar time vs month, (b) duration (h) vs month, and (c) duration (h) vs local solar time. (d)–(f) As in (a)–(c), but for the TC-induced EXHP. In (a), (b), (d), and (e), the values are averaged for each 10- (or 11-) day period in JJA (e.g., 1–10 Jun, 11–20 Jun, 21–30 Jun, 21–31 Jul).

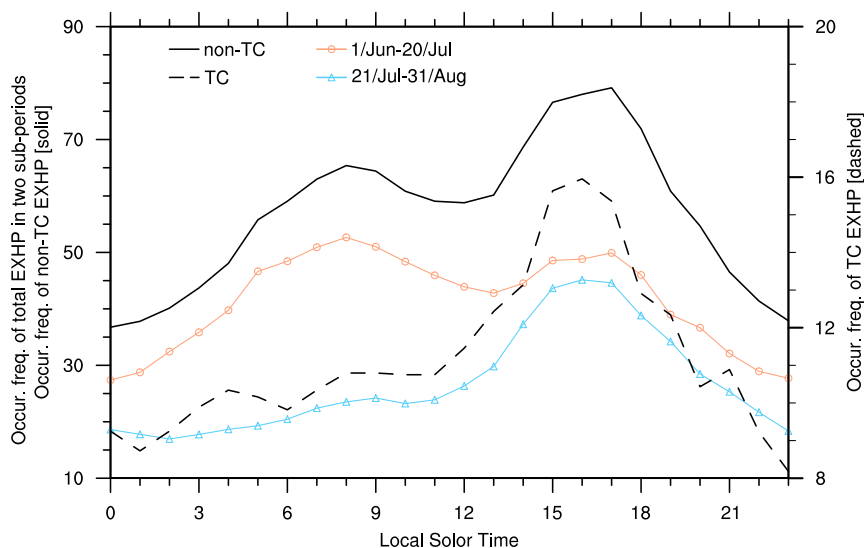


FIG. 5. Diurnal variation of the occurrence frequency (hr^{-1}) of EXHP during the 1975–2018 summers. Note that separate y axis is used for the TC-induced EXHP illustrated by dashed line. Solid black line denotes non-TC EXHP, and total EXHP amounts during 1 Jun–20 Jul and 21 Jul–31 Aug are represented by orange and blue lines, respectively.

over the YRD region (Figs. 7d,e). Enhancement in the EXHP intensity during the latter era is observed at more locations over the region than those with weakened EXHP intensities (Fig. 7i). Prominent increases in the EXHP amount, occurrence frequency and intensity are detected over the key analysis area, especially for the first two variables in the major cities of Wuxi, Changzhou, and Nanjing. Moreover, a stronger similarity is found in the pattern of differences in the EXHP occurrence frequency (rather than intensity) from that of the EXHP amount (cf. Figs. 7c,f,i).

Figure 8 shows the spatial distributions of trends derived from OLS regression in the amount, occurrence frequency, and intensity of all, non-TC, and TC-induced EXHP, respectively. Stations that pass the significance test at 90% (99%) confidence level are labeled as smaller (larger) gray dots. For all EXHP (including both non-TC and TC-induced EXHP), stations with statistically significant increasing trends in the amount and occurrence frequency are mostly located within the key analysis area (Figs. 8a,d). Neutral trends in precipitation intensity are observed at most stations, except for several stations with significant positive trends within the key analysis area. A comparison of Figs. 7 and 8 reveals that the increased EXHP amount over the YRD urban areas are contributed more by the higher occurrence frequency than the enhanced intensity. Note that the less evident intensity trend detected at central Shanghai differs somewhat from that found by Liang and Ding (2017), due to the use of different EXHP definitions and

analysis periods. When the TC-induced EXHP are excluded, the increasing trends in the amount, occurrence frequency, and intensity of the non-TC EXHP over the YRD urban areas are still evident (Figs. 8b,e,h), albeit with smaller magnitudes than those of all the EXHP (Figs. 8a,d,g). The TC-induced EXHP amount (Fig. 8c) shows significant increasing trends over the YRD region, with stations that pass the significance test mostly (15 out of 23) located within the key analysis area. Similar features are found in the occurrence frequency (Fig. 8f). Although larger increasing trends in the TC-induced EXHP intensity than the non-TC EXHP intensity are found over the central portion of the key analysis area, only a few stations pass the significance tests (cf. Figs. 8h,i).

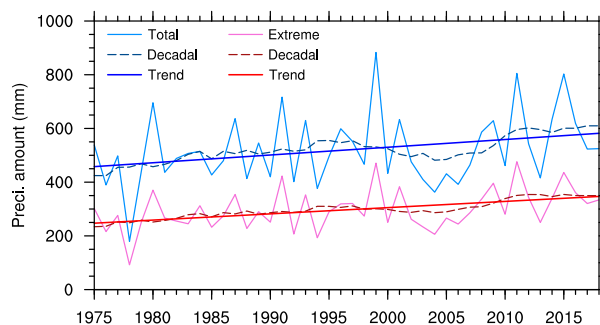


FIG. 6. Annual evolution during 1975–2018 of the total summer-averaged precipitation (light blue) and EXHP (light red) amounts (mm) from the 70 national surface stations over the YRD region. Dashed and dark solid lines denote decadal and trend components, respectively.

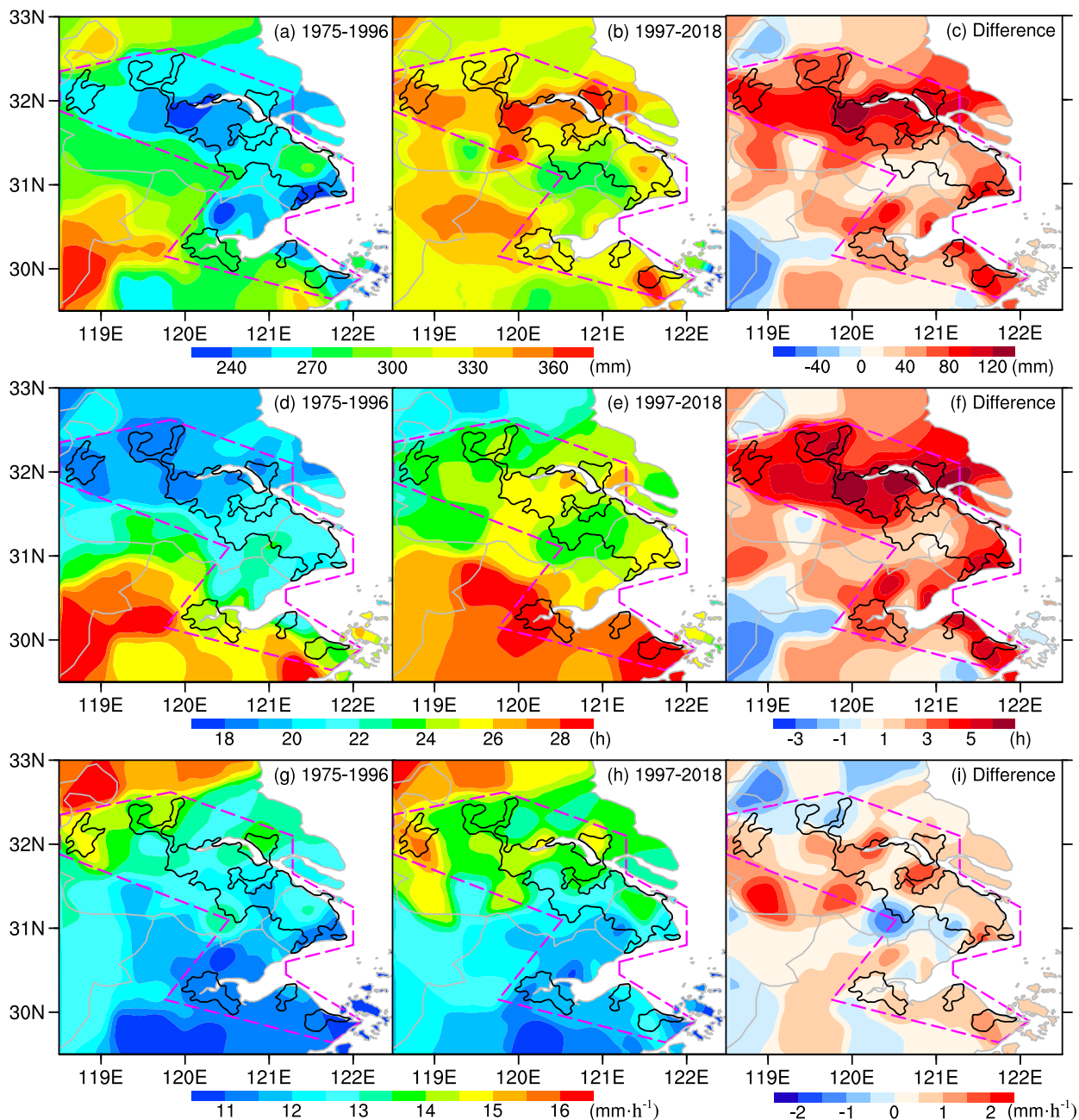


FIG. 7. (top) Spatial distributions of the EXHP amount (mm), (middle) occurrence frequency (h), and (bottom) intensity (mm h^{-1}) during the JJA of (a),(d),(g) 1975-96 and (b),(e),(h) 1997-2018. (c),(f),(i) The difference between (b) and (a), between (e) and (d), and between (h) and (g), respectively.

Figure 9 provides the linear trends in EXHP at urban and rural stations derived from quantile regression. Results show consistently larger increasing trends in all and non-TC EXHP amount and occurrence frequency (Figs. 9a,b,d,e) for almost all the quantiles over urban stations than rural stations, with small differences in trends for TC-induced EXHP amount and occurrence frequency (Figs. 9c,f). Moreover, the urban-vs-rural

differences in trends are much more prominent for larger quantiles. In contrast, there are remarkable differences in TC-induced EXHP intensity between urban and rural stations, with larger increasing trends over urban stations (Fig. 9i), but with minor differences in TC-induced EXHP amount and occurrence frequency (Figs. 9g,h). A comparison of Figs. 8 and 9 shows that the OLS and quantile regression results are qualitatively

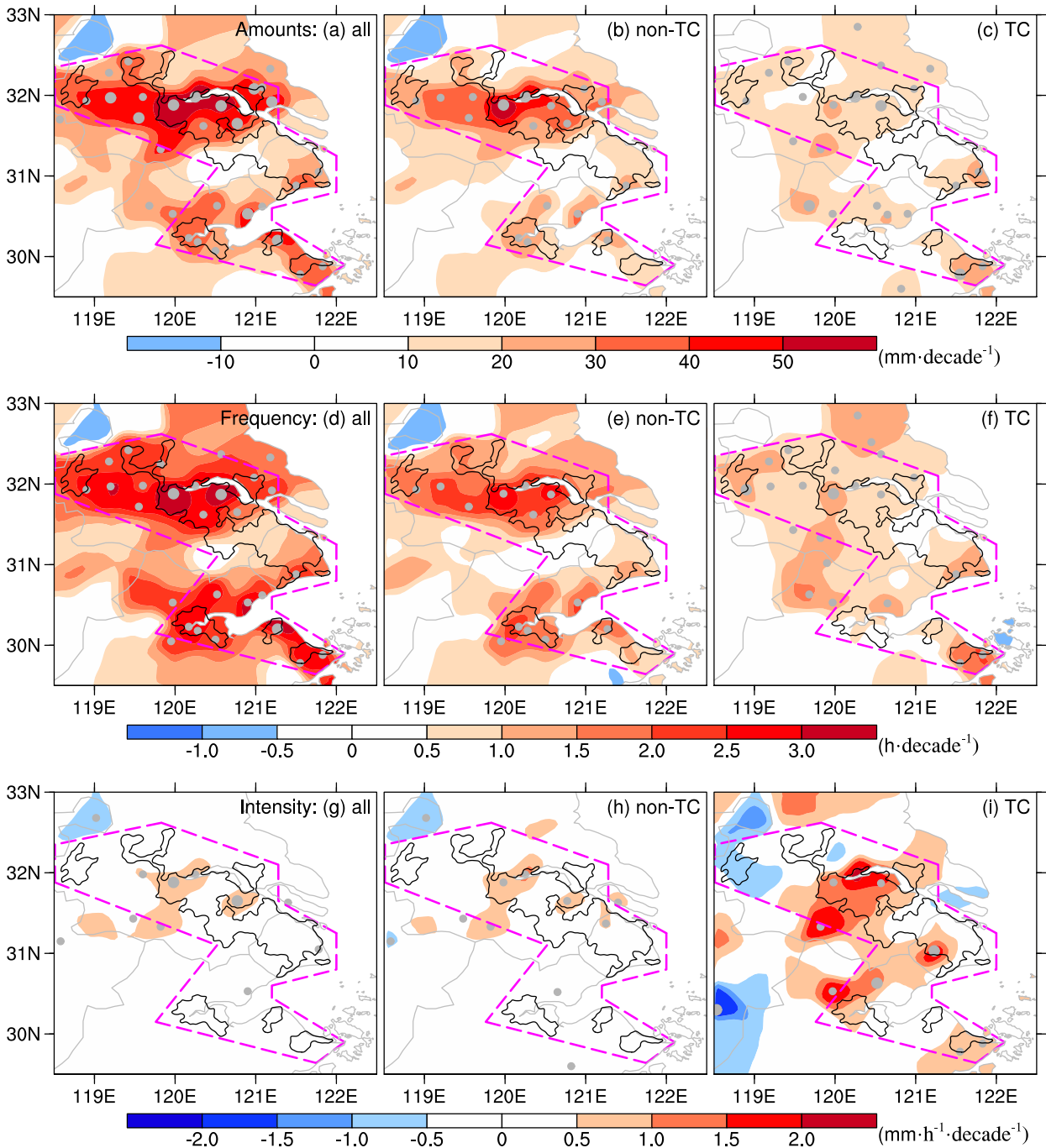


FIG. 8. OLS regression slopes of the EXHP (a) amount (mm decade^{-1}), (d) occurrence frequency (h decade^{-1}), and (g) intensity ($\text{mm h}^{-1} \text{decade}^{-1}$) during the 1975–2018 summers. (b), (e), (h) As in (a), (d), (g), but for the non-TC EXHP. (c), (f), (i) As in (a), (d), (g), but for the TC-induced EXHP. Larger and smaller gray dots denote stations with significant trends at 99% and 90% confidence level, respectively.

consistent and that the OLS regression slopes look like the regression results derived from the 0.5 quantile. These results collectively indicate that the YRD urban agglomeration might have contributed to the intensification of both non-TC and TC-induced hourly

precipitation, leading to more occurrences of EXHP, which are qualitatively consistent with the previous finding about rainfall enhancement caused by Hurricane Harvey (2017) in Houston (Zhang et al. 2018). On the other hand, Wu et al. (2019) note that the TC-induced EXHP over the

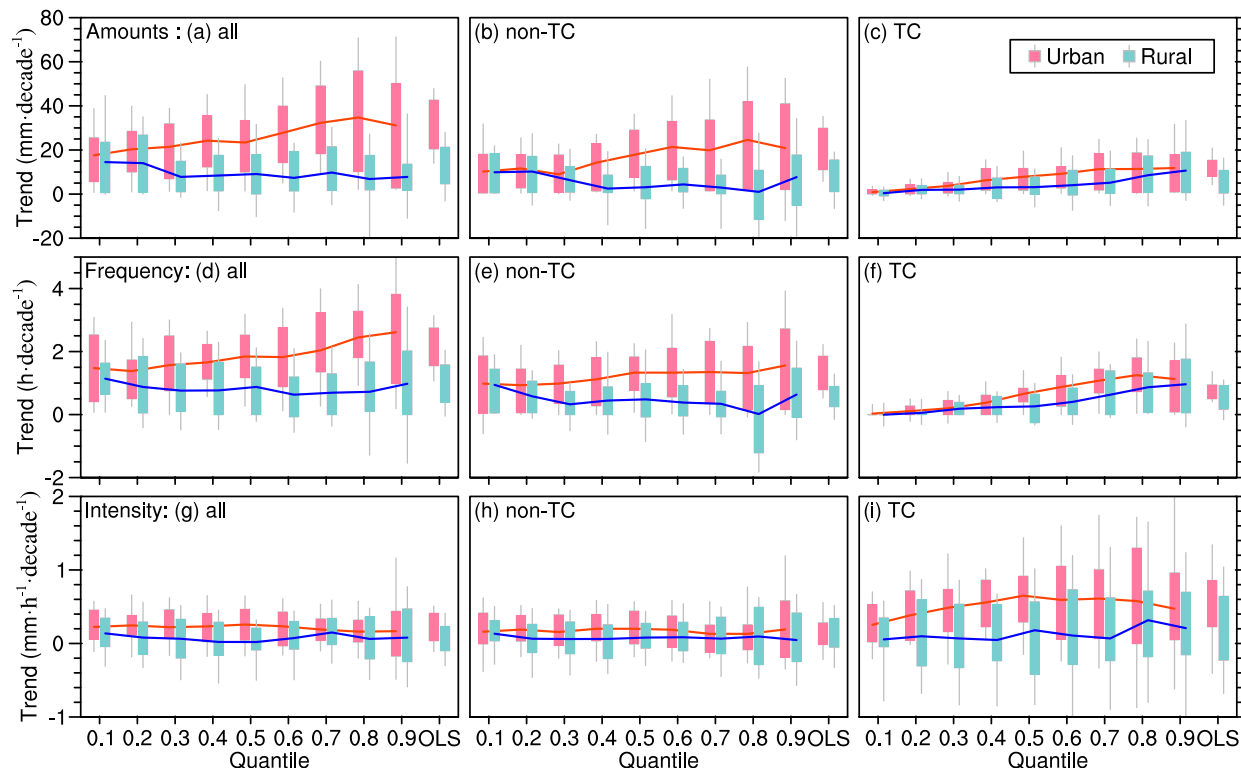


FIG. 9. Box-and-whisker plots of the quantile regression slopes of EXHP (a) amount (mm decade^{-1}), (d) occurrence frequency (h decade^{-1}), and (g) intensity ($\text{mm h}^{-1} \text{decade}^{-1}$) during the 1975–2018 summers. (b),(e),(h) As in (a),(d),(g), but for the non-TC EXHP. (c),(f),(i) As in (a),(d),(g), but for the TC-induced EXHP. The box-and-whisker plots show the interquartile range (rectangle), outliers (i.e., the 10th and 90th percentiles; whiskers), and mean (solid line). OLS regression slopes in Fig. 8 (denoted by “OLS”) are also plotted next to the 0.9 quantile for comparison.

PRD region has decreased due to substantial decreases in the number of landfalling TCs over coastal South China (Chang et al. 2012).

To further explore the possible link between the increasing precipitation amount and urbanization (i.e., in

terms of the UHI effects), we examine spatial distributions of T_{sairst} , its difference between the preurbanization and rapid urbanization eras, and its trends derived from OLS regression during 1975–2018 over the YRD region (Fig. 10). In general, the daily temperature decreases

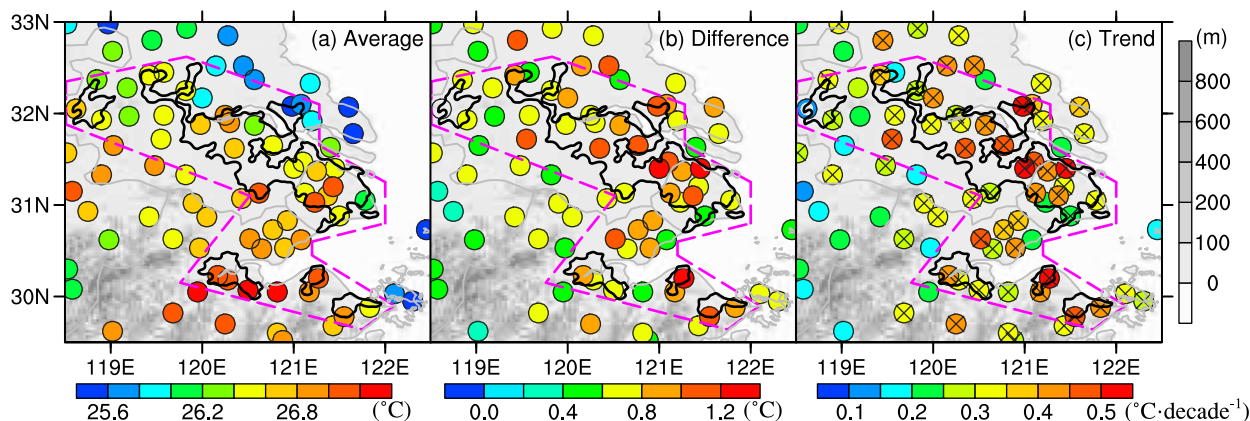


FIG. 10. Spatial distributions of (a) daily surface air temperature (T_{sairst} ; $^{\circ}\text{C}$) averaged during the 1975–2018 summers, (b) summer T_{sairst} difference ($^{\circ}\text{C}$) between 1997–2018 and 1975–96, and (c) OLS regression slopes ($^{\circ}\text{C decade}^{-1}$) of summer T_{sairst} during 1975–2018, with crosses denoting the trend significance at 99% confidence level. Gray shading represents topography (m).

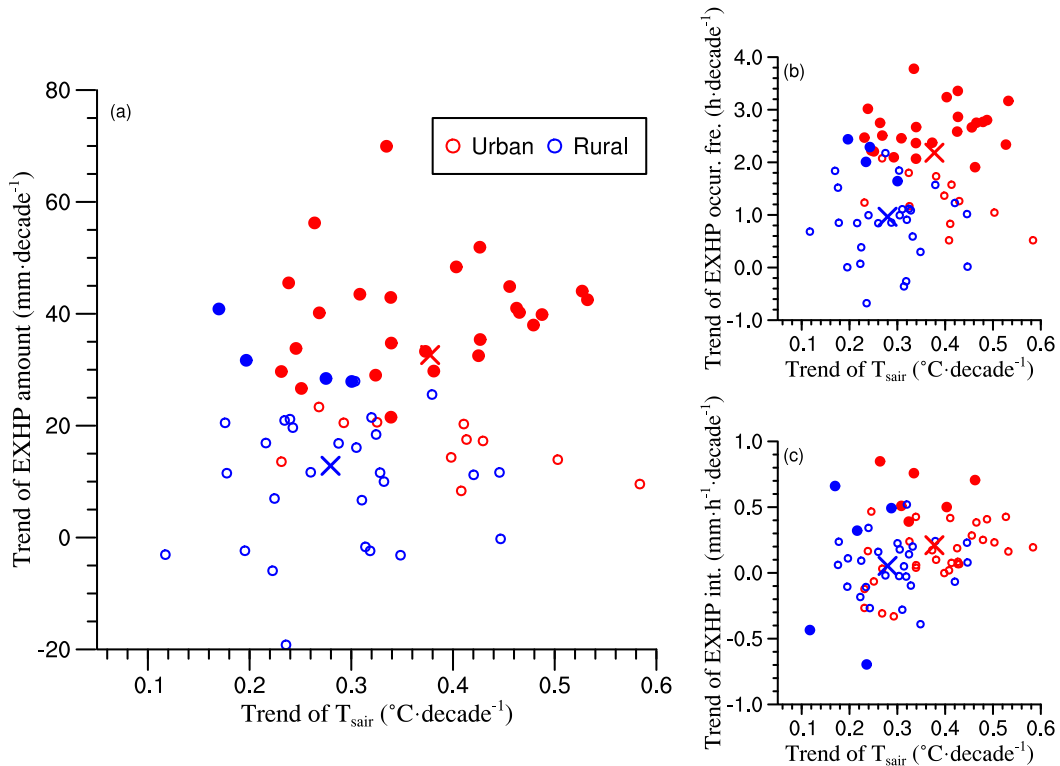


FIG. 11. Scatterplots of the trends of T_{sair} vs those of the EXHP (a) amount, (b) occurrence frequency, and (c) intensity. Red and blue colors denote the urban and rural stations, i.e., stations within and outside the key analysis area in Fig. 1b, respectively. Filled circles denote stations where trends of the EXHP variable passed the significant test at 90% confidence level. Crosses represent mean values among the urban and rural stations, respectively. Differences in the mean values of T_{sair} , EXHP amount, occurrence frequency and intensity between urban and rural stations are significant at 99% confidence level with a t test. The trends are derived from OLS regression.

with latitude with a warm center at the southeast of the key analysis area (Fig. 10a). Of particular relevance are that T_{sair} become higher during the rapid urbanization era (i.e., positive differences shown in Fig. 10b) and that significant increasing trends are detected at almost all the stations over the YRD region (Fig. 10c). The increasing trends in T_{sair} are higher than $0.3^{\circ}\text{C decade}^{-1}$ over the urban areas, except for the city of Nanjing located in the northwest of the key analysis area. In the major cities of Shanghai, Suzhou, Wuxi, and Ningbo with rapid urban expansion in the last several decades (Fig. 1), the T_{sair} trends reach $0.45^{\circ}\text{C decade}^{-1}$. These trends are much larger than the global mean value, with approximately an increase of 1.53°C in the mean land T_{sair} from 1850–1900 to 2006–15 (IPCC 2019). This suggests a warmer environment contributed by the UHI effects in addition to global warming, which is consistent with previous findings (e.g., Zhou et al. 2004).

Figure 11 further shows the relationship between the trends in T_{sair} and EXHP amount/frequency/intensity but at individual stations. The urban-vs-rural differences in the trends of area-averaged temperature, and EXHP

amount, occurrence frequency, and intensity are all significant at 99% confidence level with a t test. Under the background of global warming, the T_{sair} trends at all the stations are positive, with the mean trend at the urban stations ($0.38^{\circ}\text{C decade}^{-1}$) being larger than that at the rural stations ($0.28^{\circ}\text{C decade}^{-1}$), clearly reflecting the UHI impacts. The trends in EXHP amount (JJA accumulation) are mostly positive, which is qualitatively consistent with the previous study of Xiao et al. (2016). Of importance is that larger trends in the EXHP amount are observed at the urban stations than those at the rural stations, with mean trends of 32.6 and $12.8\text{mm decade}^{-1}$, respectively (Fig. 11a). The overall pattern of the EXHP occurrence frequency and T_{sair} (Fig. 11b) resembles that of the EXHP amount and T_{sair} (Fig. 11a), with larger trends for urban stations. This is not exactly the case for the EXHP intensity– T_{sair} diagram (Fig. 11c), showing much less organized intensity trend distributions between the urban and rural stations. Despite the less organized distributions, most urban stations still exhibit larger EXHP intensity trends. Collectively, all these larger trends at the urban stations than the rural stations indicate possible contribution of the

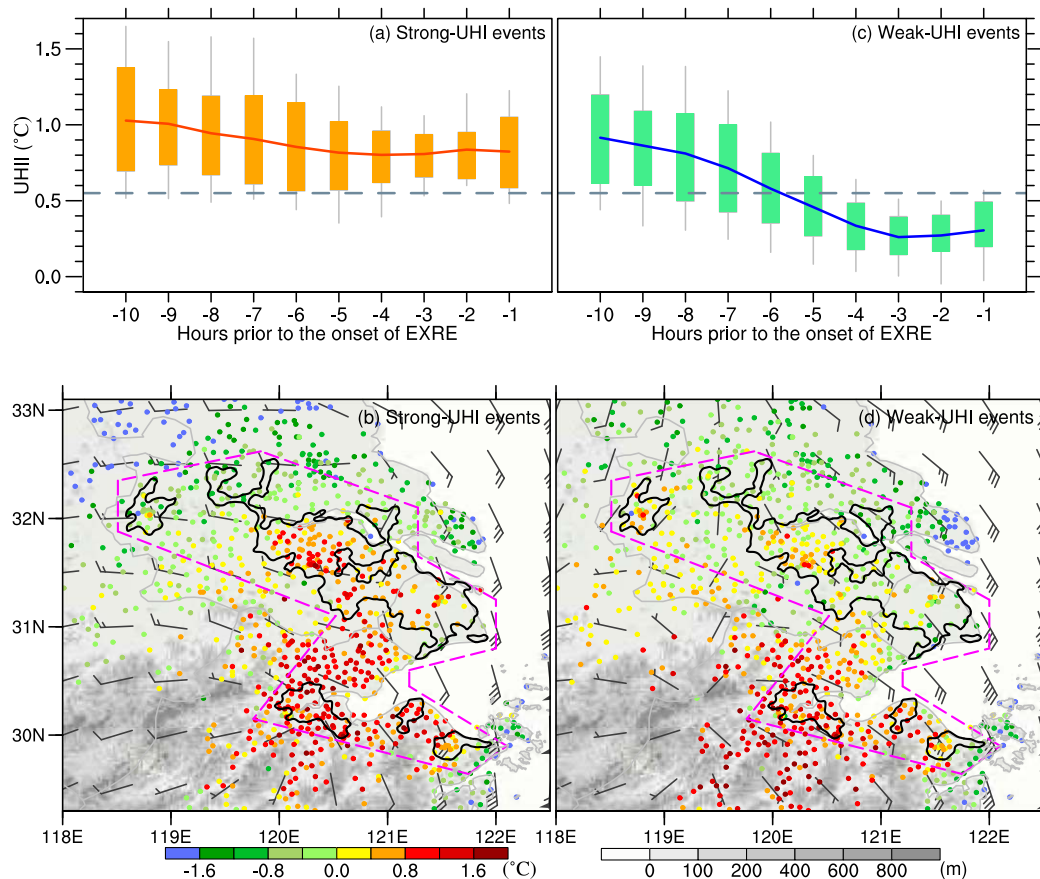


FIG. 12. (a) Box-and-whisker plots of the UHII for the identified strong-UHI EXREs, showing the interquartile range (rectangle), outliers (i.e., the 10th and 90th percentiles; whiskers), and mean (solid line). (b) Composite pre-event surface air temperature (T_{sair}) perturbation (ΔT ; $^{\circ}\text{C}$; dots), and 975-hPa horizontal winds (a full barb is 1 m s^{-1}) for the strong-UHI EXREs. The hourly temperature observations in the 3-h period before each EXRE's onset and 6-h-interval ERA-interim data at 1400 LST of the day each EXRE occurred are used in the calculation. (c),(d) As in (a) and (b), but for the identified weak-UHI EXREs. Stations with altitudes $> 100 \text{ m}$ above the mean sea level are not shown in (b) and (d).

UHI effects to more frequent occurrence of EXHP over the YRD urban agglomeration.

In summary, the total EXHP amount in summer has increased substantially during the rapid urbanization era (1997–2018) relative to the preurbanization era (1975–96) over the YRD region. The statistically significant increasing trends in both amount and occurrence frequency of the EXHP, including non-TC and TC-induced EXHP, are mostly observed over the urban agglomeration, and they are generally larger than those over the nearby rural areas. In addition, larger trends in T_{sair} are also observed at the urban stations than the rural stations.

5. Contrasting strong- versus weak-UHI EXREs in 2011–18

It is shown from the preceding section that there exists a possible relationship between the statistically significant

increases in EXHP and the rapid urbanization (i.e., reflected by the UHI effects) over the YRD urban agglomeration. To confirm this result, 113 locally developed non-TC EXREs detected by dense AWSs and 10-min mosaic radar images over the key analysis area during 2011–18 summers are analyzed. To this end, the 113 EXREs are categorized into 56 strong- and 57 weak-UHI events, as described in section 2b. It is evident from Fig. 12a that the hourly UHII values for the strong-UHI events are mostly greater than the multiyear averaged UHII ($\text{UHII}_{\text{mean}} = 0.55^{\circ}\text{C}$) during the 10-h preonset period, and exhibit little changes 5 h prior to the onset of the EXREs. Prominent warm centers are observed over the central portion of the band-shaped urban region, the Hangzhou area, and the areas between them where numerous scattered urban lands are located (Fig. 12b). These warm centers generally collocate with the larger/higher EXHP amounts/frequencies during the rapid-urbanization era relative to

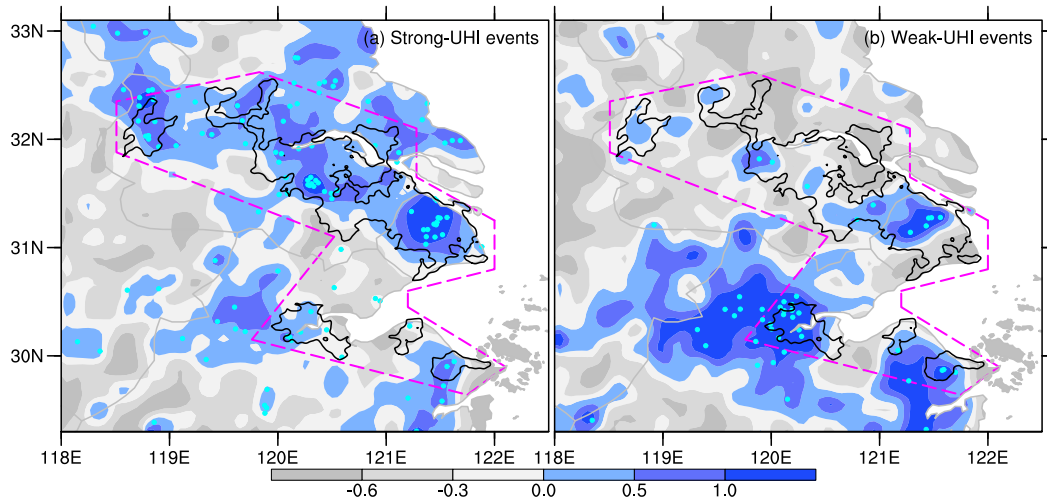


FIG. 13. Composite spatial distributions of the region-normalized precipitation amount (shading) of the 2011–18 EXREs with (a) strong UHI and (b) weak UHI, respectively. Cyan dots denote stations with hourly precipitation records $\geq 23.7 \text{ mm h}^{-1}$ occurring more than twice.

the preurbanization era (cf. Figs. 12b and 7), and the significant, large increasing trends of EXHP during 1975–2018 (cf. Figs. 12b and 8a,d). Note that the relatively weaker warm centers at Shanghai and Nanjing (Fig. 12a) are probably attributed to the advection of unheated air over ocean and rural areas (D.-L. Zhang et al. 2009), respectively, as indicated by the low-level southeasterly and westerly winds.

Prior to the onset of the identified weak-UHI events, the UHI intensity weakens continuously and most of the UHI values become smaller than $\text{UHII}_{\text{mean}}$ in 4 h before their onset (Fig. 12c). The prominent warm centers prior to the onset of EXREs in the strong-UHI events (Fig. 12b) are hardly present in the weak-UHI events (Fig. 12d). Over the band-shaped urban region and the Nanjing area, lower positive ΔT values are scattered over a few city centers only, whereas higher positive ΔT values concentrate in the southern portion of the key analysis area (i.e., the Hangzhou area) and nearby mountains. This indicates more favorable thermodynamic conditions (i.e., more unstable) over the Hangzhou area and nearby mountains than the band-shaped urban region to the north.

Figure 13 shows the spatial distributions of the region-normalized precipitation amount, calculated by Eq. (2), during the strong- and weak-UHI EXREs, respectively. For the strong-UHI EXREs, the EXHP records ($\geq 23.7 \text{ mm h}^{-1}$) and prominent positive rainfall accumulations are mostly observed over the band-shaped urban region and its nearby Nanjing area, where prominent warm centers are observed (Fig. 12b). Two separate rainfall centers with smaller spatial coverages are found over Mt. Tianmu and Ningbo, respectively. In contrast, the hourly extremes and prominent positive

rainfall accumulation during the weak-UHI EXREs are mostly produced over western Hangzhou (Fig. 13b), due likely to lifting of the unstable southeasterly flow by the complex terrain (Fig. 12d). Over the band-shaped urban region, only scattered rainfall centers are found (Fig. 13b), coinciding roughly with the isolated warm centers (Fig. 12d). Considering that UHI is calculated by area-averaged temperature differences, there might be some mismatch between Figs. 12 and 13, such as the inconsistency between temperature perturbation and region-normalized precipitation over Hangzhou for the strong-UHI events.

The above results suggest that the strong UHI effects over the YRD region (i.e., the prominent warm centers over the central key analysis area) could contribute to the increased occurrence frequency of summer EXHP over the densely populated urban agglomeration. Situated near the coast and with mountains adjacent to its southern boundary, the urban agglomeration over the YRD region can be influenced by land–sea breezes and mountain–plain circulations, as in other urban areas in the world (Shepherd and Burian 2003; Wang et al. 2014; Chen et al. 2016; Wu and Luo 2016; Li et al. 2017a; Zhang 2020). This may change local thermal conditions and near-surface airflows, and consequently influence the initiation and development of convective storms. Interactions between the resultant local circulations, and their influences on the EXREs over the YRD region, under the background of global warming, deserve further studies.

6. Summary and concluding remarks

In this study, we present a climatology of the summertime (JJA) EXHP over the YRD region during

1975–2018, using hourly precipitation observations and historical land-use data, and then examine the relationship between the EXHP changes and rapid urbanization since the middle 1990s. Some major results are summarized as follows.

The EXHP over the YRD region shows distinct characteristics during the early and late summer. Namely, it is produced mostly (95%) by non-TC systems (e.g., low-level shear lines, vortices) along mei-yu fronts or locally developed convective storms due to the increasing surface heating during the early summer (Luo et al. 2016). Its diurnal variations exhibit double peaks: a major peak in the morning and a secondary peak in the afternoon. In contrast, the EXHP during later summers is produced by both non-TC systems (66%) and TCs (34%). The former occurs mostly in the afternoon with short durations (≤ 12 h), whereas the latter features a prominent afternoon peak.

Although a high correlation between larger amount or higher occurrence frequency of precipitation averaged during the 1975–2018 summers and urban areas is not found, we note substantial increases in both the amount and the occurrence frequency of the non-TC and TC-induced EXHP over the YRD region during the rapid-urbanization era (i.e., 1997–2018), as compared to the preurbanization era (i.e., 1975–96). Statistically significant increasing trends in the EXHP amount and occurrence frequency during the 1975–2018 summers are observed at most stations over the YRD urban areas, but significant trends in the EXHP intensity have lower magnitudes and are observed at much fewer stations. Moreover, the significant increasing trends of EXHP generally collocate with significant increasing trends of surface air temperature, with larger trends in both variables at urban stations than rural stations, suggesting the presence of a relationship between the EXHP increases and the UHI effects.

An analysis of 113 locally developed non-TC EXRES over the YRD region during 2011–18 summers reveals contrasting rainfall distributions between the strong- and weak-UHI events. EXHP is mostly produced over the urban areas, especially a band-shaped urban region during the strong-UHI events, whereas it is mainly distributed over the mountains in southern YRD region during the weak-UHI events.

In conclusion, we may state that the summertime EXHP over the densely populated urban agglomeration of the YRD region has shown significant increases during the past half a century as a result of rapid urbanization, in addition to global warming. This result adds new supporting evidence to the findings from the recent studies of Liang and Ding (2017), Fu et al. (2019), and Wu et al. (2019), who showed the correlation

between rapid urbanization and more extreme rainfall events over the coastal urban agglomerations in South and East China. Of course, more studies are needed to better understand the associated physical mechanisms governing the subdaily extreme precipitation-producing storms, particularly the interactive roles of the circulations induced by urbanization, land–sea contrasts, and orography under various larger-scale conditions in a warming climate.

Acknowledgments. This work was jointly supported by the National Key Research and Development Program of China (2018YFC1507400), National Natural Science Foundation of China (41775050), and the Basic Research and Operation Funding of Chinese Academy of Meteorological Sciences (CAMS) (2017Z006). We would like to acknowledge Dr. Fumin Ren of CAMS for his assistance in using OSAT to identify the TC-induced precipitation. Special thanks go to the Shanghai Typhoon Institute of China Meteorological Administration for the TC information used in this study.

REFERENCES

- Bowman, K. P., and M. D. Fowler, 2015: The diurnal cycle of precipitation in tropical cyclones. *J. Climate*, **28**, 5325–5334, <https://doi.org/10.1175/JCLI-D-14-00804.1>.
- Cao, L., Y. Zhu, G. Tang, F. Yuan, and Z. Yan, 2016: Climatic warming in China according to a homogenized data set from 2419 stations. *Int. J. Climatol.*, **36**, 4384–4392, <https://doi.org/10.1002/joc.4639>.
- Chang, C.-P., Y. Lei, C.-H. Sui, X. Lin, and F. Ren, 2012: Tropical cyclone and extreme rainfall trends in East Asian summer monsoon since mid-20th century. *Geophys. Res. Lett.*, **39**, L18702, <https://doi.org/10.1029/2012GL052945>.
- Changnon, S. A., 1968: The LaPorte weather anomaly—Fact or fiction? *Bull. Amer. Meteor. Soc.*, **49**, 4–11, <https://doi.org/10.1175/1520-0477-49.1.4>.
- , 1969: Recent studies of urban effects on precipitation in the United States. *Bull. Amer. Meteor. Soc.*, **50**, 411–421, <https://doi.org/10.1175/1520-0477-50.6.411>.
- Chen, X., F. Zhang, and K. Zhao, 2016: Diurnal variations of the land-sea breeze and its related precipitation over South China. *J. Atmos. Sci.*, **73**, 4793–4815, <https://doi.org/10.1175/JAS-D-16-0106.1>.
- Chen, Y., P. Zhai, and B. Zhou, 2018: Detectable impacts of the past half-degree global warming on summertime hot extremes in China. *Geophys. Res. Lett.*, **45**, 7130–7139, <https://doi.org/10.1029/2018GL079216>.
- Cressman, G. P., 1959: An operational objective analysis system. *Mon. Wea. Rev.*, **87**, 367–374, [https://doi.org/10.1175/1520-0493\(1959\)087<0367:AOOAS>2.0.CO;2](https://doi.org/10.1175/1520-0493(1959)087<0367:AOOAS>2.0.CO;2).
- Ding, Y., 1992: Summer monsoon rainfalls in China. *J. Meteor. Soc. Japan*, **70**, 373–396, https://doi.org/10.2151/jmsj1965.70.1B_373.
- Dou, J., Y. Wang, R. Bornstein, and S. Miao, 2015: Observed spatial characteristics of Beijing urban climate impacts on summer thunderstorms. *J. Appl. Meteor. Climatol.*, **54**, 94–105, <https://doi.org/10.1175/JAMC-D-13-0355.1>.
- Friederichs, P., and A. Hense, 2007: Statistical downscaling of extreme precipitation events using censored quantile

- regression. *Mon. Wea. Rev.*, **135**, 2365–2378, <https://doi.org/10.1175/MWR3403.1>.
- Fu, X., X.-Q. Yang, and X. Sun, 2019: Spatial and diurnal variations of summer hourly rainfall over three super city clusters in eastern China and their possible link to the urbanization. *J. Geophys. Res. Atmos.*, **124**, 5445–5462, <https://doi.org/10.1029/2019JD030474>.
- IPCC, 2019: Climate change and land: An IPCC special report on climate change, desertification, land degradation, sustainable land management, food security, and greenhouse gas fluxes in terrestrial ecosystems. IPCC, 1542 pp., <https://www.ipcc.ch/site/assets/uploads/2019/08/Fullreport-1.pdf>.
- Jin, M., and J. M. Shepherd, 2008: Aerosol relationships to warm season clouds and rainfall at monthly scales over East China: Urban land versus ocean. *J. Geophys. Res.*, **113**, D24S90, <https://doi.org/10.1029/2008JD010276>.
- Kaufmann, R. K., K. C. Seto, A. Schneider, Z. Liu, L. Zhou, and W. Wang, 2007: Climate response to rapid urban growth: Evidence of a human-induced precipitation deficit. *J. Climate*, **20**, 2299–2306, <https://doi.org/10.1175/JCLI4109.1>.
- Kishtawal, C. M., D. Niyogi, M. Tewari, R. A. Pielke Sr., and J. M. Shepherd, 2010: Urbanization signature in the observed heavy rainfall climatology over India. *Int. J. Climatol.*, **30**, 1908–1916, <https://doi.org/10.1002/joc.2044>.
- Koenker, R., and G. Bassett, 1978: Regression quantiles. *Econometrica*, **46**, 33–50, <https://doi.org/10.2307/1913643>.
- Lei, M., D. Niyogi, C. Kishtawal, R. A. Pielke Sr., A. Beltran-Przekurat, T. E. Nobis, and S. S. Vaidya, 2008: Effect of explicit urban land surface representation on the simulation of the 26 July 2005 heavy rain event over Mumbai, India. *Atmos. Chem. Phys.*, **8**, 5975–5995, <https://doi.org/10.5194/acp-8-5975-2008>.
- Li, H., X. Cui, and D.-L. Zhang, 2017a: On the initiation of an isolated heavy-rain-producing storm near the central urban area of Beijing metropolitan region. *Mon. Wea. Rev.*, **145**, 181–197, <https://doi.org/10.1175/MWR-D-16-0115.1>.
- , —, and —, 2017b: Sensitivity of the initiation of an isolated thunderstorm over the Beijing metropolitan region to urbanization, terrain morphology and cold outflows. *Quart. J. Roy. Meteor. Soc.*, **143**, 3153–3164, <https://doi.org/10.1002/qj.3169>.
- Li, W., S. Chen, G. Chen, W. Sha, C. Luo, Y. Feng, Z. Wen, and B. Wang, 2011: Urbanization signatures in strong versus weak precipitation over the Pearl River Delta metropolitan regions of China. *Environ. Res. Lett.*, **6**, 049503, <https://doi.org/10.1088/1748-9326/6/4/049503>.
- Li, Z., X. Deng, F. Wu, and S. S. Hasan, 2015: Scenario analysis for water resources in response to land use change in the middle and upper reaches of the Heihe River basin. *Sustainability*, **7**, 3086–3108, <https://doi.org/10.3390/su7033086>.
- Liang, P., and Y. Ding, 2017: The long-term variation of extreme heavy precipitation and its link to urbanization effects in Shanghai during 1916–2014. *Adv. Atmos. Sci.*, **34**, 321–334, <https://doi.org/10.1007/s00376-016-6120-0>.
- Lin, C.-Y., W.-C. Chen, P.-L. Chang, and Y.-F. Sheng, 2011: Impact of the urban heat island effect on precipitation over a complex geographic environment in northern Taiwan. *J. Appl. Meteor. Climatol.*, **50**, 339–353, <https://doi.org/10.1175/2010JAMC2504.1>.
- Liu, J., and Coauthors, 2014: Spatiotemporal characteristics, patterns, and causes of land-use changes in China since the late 1980s. *J. Geogr. Sci.*, **24**, 195–210, <https://doi.org/10.1007/s11442-014-1082-6>.
- Luo, X., M. Xue, and J. Fei, 2018: Simulation and analysis of the initiation of a squall line within a meiyu frontal system in East China. *Atmosphere*, **9**, 183, <https://doi.org/10.3390/atmos9050183>.
- Luo, Y., H. Wang, R. Zhang, W. Qian, and Z. Luo, 2013: Comparison of rainfall characteristics and convective properties of monsoon precipitation systems over South China and the Yangtze and Huai River basin. *J. Climate*, **26**, 110–132, <https://doi.org/10.1175/JCLI-D-12-00100.1>.
- , M. Wu, F. Ren, J. Li, and W.-K. Wong, 2016: Synoptic situations of extreme hourly precipitation over China. *J. Climate*, **29**, 8703–8719, <https://doi.org/10.1175/JCLI-D-16-0057.1>.
- Miao, S., F. Chen, Q. Li, and S. Fan, 2011: Impacts of urban processes and urbanization on summer precipitation: A case study of heavy rainfall in Beijing on 1 August 2006. *J. Appl. Meteor. Climatol.*, **50**, 806–825, <https://doi.org/10.1175/2010JAMC2513.1>.
- Mishra, V., J. M. Wallace, and D. P. Lettenmaier, 2012: Relationship between hourly extreme precipitation and local air temperature in the United States. *Geophys. Res. Lett.*, **39**, L16403, <https://doi.org/10.1029/2012GL052790>.
- NCC, 1998: *China's 1998 Severe Flood and Climate Extremes* (in Chinese). China Meteorological Press, 137 pp.
- Niyogi, D., P. Pyle, M. Lei, S. P. Arya, C. M. Kishtawal, M. Shepherd, F. Chen, and B. Wolfe, 2011: Urban modification of thunderstorms: An observational storm climatology and model case study for the Indianapolis urban region. *J. Appl. Meteor. Climatol.*, **50**, 1129–1144, <https://doi.org/10.1175/2010JAMC1836.1>.
- Ntelekos, A. A., J. A. Smith, L. Donner, J. D. Fast, W. I. Gustafson Jr., E. G. Chapman, and W. F. Krajewski, 2009: The effects of aerosols on intense convective precipitation in the northeastern United States. *Quart. J. Roy. Meteor. Soc.*, **135**, 1367–1391, <https://doi.org/10.1002/qj.476>.
- Paul, S., S. Ghosh, M. Mathew, A. Devanand, S. Karmakar, and D. Niyogi, 2018: Increased spatial variability and intensification of extreme monsoon rainfall due to urbanization. *Sci. Rep.*, **8**, 3918, <https://doi.org/10.1038/s41598-018-22322-9>.
- Ren, F., G. Wu, W. Dong, X. Wang, Y. Wang, W. Ai, and W. Li, 2006: Changes in tropical cyclone precipitation over China. *Geophys. Res. Lett.*, **33**, L20702, <https://doi.org/10.1029/2006GL027951>.
- , Y. Wang, X. Wang, and W. Li, 2007: Estimating tropical cyclone precipitation from station observations. *Adv. Atmos. Sci.*, **24**, 700–711, <https://doi.org/10.1007/s00376-007-0700-y>.
- Rosenfeld, D., 2000: Suppression of rain and snow by urban and industrial air pollution. *Science*, **287**, 1793–1796, <https://doi.org/10.1126/science.287.5459.1793>.
- Shastri, H., S. Paul, S. Ghosh, and S. Karmakar, 2015: Impacts of urbanization on Indian summer monsoon rainfall extremes. *J. Geophys. Res. Atmos.*, **120**, 496–516, <https://doi.org/10.1002/2014JD022061>.
- Shepherd, J. M., 2005: A review of current investigations of urban-induced rainfall and recommendations for the future. *Earth Interact.*, **9**, <https://doi.org/10.1175/EI156.1>.
- , and S. J. Burian, 2003: Detection of urban induced rainfall anomalies in a major coastal city. *Earth Interact.*, **7**, [https://doi.org/10.1175/1087-3562\(2003\)007<0001:DOUIRA>2.0.CO;2](https://doi.org/10.1175/1087-3562(2003)007<0001:DOUIRA>2.0.CO;2).
- Tuleya, R. E., 1994: Tropical storm development and decay: Sensitivity to surface boundary conditions. *Mon. Wea. Rev.*, **122**, 291–304, [https://doi.org/10.1175/1520-0493\(1994\)122<0291:TSDADS>2.0.CO;2](https://doi.org/10.1175/1520-0493(1994)122<0291:TSDADS>2.0.CO;2).
- Wan, H., Z. Zhong, X. Yang, and X. Li, 2013: Impact of city belt in Yangtze River Delta in China on a precipitation process in

- summer: A case study. *Atmos. Res.*, **125–126**, 63–75, <https://doi.org/10.1016/j.atmosres.2013.02.004>.
- Wang, H., Y. Luo, and B. J.-D. Jou, 2014: Initiation, maintenance, and properties of convection in an extreme rainfall event during SCMREX: Observational analysis. *J. Geophys. Res. Atmos.*, **119**, 13 206–13 232, <https://doi.org/10.1002/2014JD022339>.
- Wang, X., P. Xiao, X. Feng, and H. Li, 2013: Extration of large-scale urban area information in China using DMSP/OLS nighttime light data (in Chinese). *Remote Sens. Land Resour.*, **25**, 159–164.
- Wu, M., and Y. Luo, 2016: Mesoscale observational analysis of lifting mechanism of a warm-sector convective system producing the maximal daily precipitation in China mainland during pre-summer rainy season of 2015. *J. Meteor. Res.*, **30**, 719–736, <https://doi.org/10.1007/s13351-016-6089-8>.
- , —, F. Chen, and W. K. Wong, 2019: Observed link of extreme hourly precipitation changes to urbanization over coastal south China. *J. Appl. Meteor. Climatol.*, **58**, 1799–1819, <https://doi.org/10.1175/JAMC-D-18-0284.1>.
- Xiao, C., P. Wu, L. Zhang, and L. Song, 2016: Robust increase in extreme summer rainfall intensity during the past four decades observed in China. *Sci. Rep.*, **6**, 38 506, <https://doi.org/10.1038/srep38506>.
- Xu, W., and E. J. Zipser, 2011: Diurnal variations of precipitation, deep convection, and lighting over and east of the eastern Tibetan Plateau. *J. Climate*, **24**, 448–465, <https://doi.org/10.1175/2010JCLI3719.1>.
- Yang, P., G. Ren, and P. Yan, 2017: Evidence for a strong association of short-duration intense rainfall with urbanization in the Beijing urban area. *J. Climate*, **30**, 5851–5870, <https://doi.org/10.1175/JCLI-D-16-0671.1>.
- Yu, R., J. Li, W. Yuan, and H. Chen, 2010: Changes in characteristics of late-summer precipitation over eastern China in the past 40 years revealed by hourly precipitation data. *J. Climate*, **23**, 3390–3396, <https://doi.org/10.1175/2010JCLI3454.1>.
- , Z. Jiang, and P. Zhai, 2016: Impact of urban land-use change in eastern China on the East Asian subtropical monsoon: A numerical study. *J. Meteor. Res.*, **30**, 203–216, <https://doi.org/10.1007/s13351-016-5157-4>.
- Yu, S., 2007: Interannual variation of annual precipitation and urban effect on precipitation in the Beijing region. *Prog. Nat. Sci.*, **17**, 1042–1050.
- Yuan, W., R. Yu, H. Chen, J. Li, and M. Zhang, 2010: Subseasonal characteristics of diurnal variation in summer monsoon rainfall over central eastern China. *J. Climate*, **23**, 6684–6695, <https://doi.org/10.1175/2010JCLI3805.1>.
- Zhai, P., X. Zhang, H. Wan, and X. Pan, 2005: Trends in total precipitation and frequency of daily precipitation extremes over China. *J. Climate*, **18**, 1096–1108, <https://doi.org/10.1175/JCLI-3318.1>.
- Zhang, C., F. Chen, S. G. Miao, Q. C. Li, X. A. Xia, and C. Y. Xuan, 2009: Impacts of urban expansion and future green planting on summer precipitation in the Beijing metropolitan area. *J. Geophys. Res.*, **114**, D02116, <https://doi.org/10.1029/2008JD010328>.
- Zhang, D.-L., 2020: Rapid urbanization and more extreme rainfall events. *Sci. Bull.*, **65**, 516–518, <https://doi.org/10.1016/j.scib.2020.02.002>.
- , Y.-X. Shou, and R. R. Dickerson, 2009: Upstream urbanization exacerbates urban heat island effects. *Geophys. Res. Lett.*, **36**, L24401, <https://doi.org/10.1029/2009GL041082>.
- , M. S. Jin, Y. Shou, and C. Dong, 2019: The influences of urban building complexes on the ambient flows over the Washington–Reston region. *J. Appl. Meteor. Climatol.*, **58**, 1325–1336, <https://doi.org/10.1175/JAMC-D-19-0037.1>.
- Zhang, H., and P. Zhai, 2011: Temporal and spatial characteristics of extreme hourly precipitation over eastern China in the warm season. *Adv. Atmos. Sci.*, **28**, 1177–1183, <https://doi.org/10.1007/s00376-011-0020-0>.
- Zhang, N., and Y. Chen, 2014: A case study of the upwind urbanization influence on the urban heat island effects along the Suzhou–Wuxi corridor. *J. Appl. Meteor. Climatol.*, **53**, 333–345, <https://doi.org/10.1175/JAMC-D-12-0219.1>.
- Zhang, Q., T. Jiang, M. Gemmer, and S. Becker, 2005: Precipitation, temperature and runoff analysis from 1950 to 2002 in the Yangtze basin, China. *Hydrol. Sci. J.*, **50**, 65–80, <https://doi.org/10.1623/HYSJ.50.1.65.56338>.
- , C. Y. Xu, S. Becker, Z. X. Zhang, Y. D. Chen, and M. Coulibaly, 2009: Trends and abrupt changes of precipitation maxima in the Pearl River basin, China. *Atmos. Sci. Lett.*, **10**, 132–144, <https://doi.org/10.1002/asl.221>.
- Zhang, W., G. Villarini, G. A. Vecchi, and J. A. Smith, 2018: Urbanization exacerbated the rainfall and flooding caused by hurricane Harvey in Houston. *Nature*, **563**, 384–388, <https://doi.org/10.1038/s41586-018-0676-z>.
- Zhang, X., F. W. Zwiers, G. Li, H. Wan, and A. J. Cannon, 2017: Complexity in estimating past and future extreme short-duration rainfall. *Nat. Geosci.*, **10**, 255–259, <https://doi.org/10.1038/ngeo2911>.
- Zhang, Y., J. A. Smith, L. Luo, Z. Wang, and M. L. Baeck, 2014: Urbanization and rainfall variability in the Beijing metropolitan region. *J. Hydrometeorol.*, **15**, 2219–2235, <https://doi.org/10.1175/JHM-D-13-0180.1>.
- Zhong, S., and X.-Q. Yang, 2015: Ensemble simulations of the urban effect on a summer rainfall event in the great Beijing metropolitan area. *Atmos. Res.*, **153**, 318–334, <https://doi.org/10.1016/j.atmosres.2014.09.005>.
- , Y. Qian, C. Zhao, R. Leung, and X.-Q. Yang, 2015: A case study of urbanization impact on summer precipitation in the greater Beijing metropolitan area: Urban heat island versus aerosol effects. *J. Geophys. Res. Atmos.*, **120**, 10 903–10 914, <https://doi.org/10.1002/2015JD023753>.
- Zhou, L., R. E. Dickinson, Y. Tian, J. Fang, Q. Li, R. K. Kaufmann, C. J. Tucker, and R. B. Myneni, 2004: Evidence for a significant urbanization effect on climate in China. *Proc. Natl. Acad. Sci. USA*, **101**, 9540–9544, <https://doi.org/10.1073/pnas.0400357101>.